Ranta, Mikaela; Hinkkanen, Marko; Repo, Anna-Kaisa; Luomi, Jorma

# Small-signal analysis of a saturated induction motor

*Published in:*
Nordic Workshop on Power and Industrial Electronics (NORPIE/2008)

Published: 09/06/2008

*Document Version*
Publisher's PDF, also known as Version of record

*Please cite the original version:*
Ranta, M., Hinkkanen, M., Repo, A-K., & Luomi, J. (2008). Small-signal analysis of a saturated induction motor. In Nordic Workshop on Power and Industrial Electronics (NORPIE/2008) (pp. 8). Espoo, Finland.

# Small-Signal Analysis of a Saturated Induction Motor

Mikaela Ranta, Marko Hinkkanen, Anna-Kaisa Repo, and Jorma Luomi

Helsinki University of Technology
Department of Electrical Engineering
P.O. Box 3000, FI-02015 TKK, Finland
email: mikaela.ranta@tkk.fi

***Abstract*—Due to magnetic saturation, the small-signal admittance of an induction motor is dependent on the direction of the excitation signal. The angle-dependence of the admittance can be used in the estimation of the flux angle, and it should be taken into account when identifying motor parameters. In this paper, the small-signal admittance of a 2.2-kW induction motor is measured at different excitation frequencies and operating points. The measured admittances are compared to data obtained by means of finite element analysis (FEA). A small-signal model of the induction motor is fitted to the admittances to analyze the results. The admittances obtained from FEA and laboratory experiments correspond well to each other, particularly at low excitation frequencies.**

## I. Introduction

Induction motors are magnetically saturated at the rated flux level. The main flux path saturates as a function of the magnetizing current, but the rotor current also affects the saturation level of the main flux, particularly in motors having skewed or closed rotor slots [1], [2]. As the path of the rotor leakage flux partially coincides with the main flux path, the rotor leakage flux saturation depends on both the magnetizing current and the rotor current.

The saturation characteristics can be analyzed with the help of the small-signal admittance. When a voltage signal is injected into the stator winding, the observed response of the current is dependent on the direction of the excitation signal due to the saturation [3]. The induction motor thus seems to be salient. In addition, the rotor slotting can cause higher-order saliencies [4]. Saturation-induced saliency has been used for identifying the flux direction, e.g. [5]. Normally, the saliency is not fixed to any certain flux component. Therefore, the mechanisms of the saturation and the influence of the saturation on the small-signal admittance need to be well understood to correctly estimate the flux angle.

The motor parameters are normally identified during the start-up of the drive [6], and an adaptation mechanism can be applied to adjust the parameters during the operation of the drive [7]. The saturation should be taken into account in the identification or adaptation. Otherwise, incremental quantities might be obtained instead of the desired operating-point quantities.

In this paper, the small-signal stator admittance of a saturated induction motor is studied by means of experiments and finite element analysis (FEA). For the measurement of the small-signal admittance, an alternating voltage signal is injected into the stator winding. Both the frequency and the direction of the signal are varied. A small-signal motor model [8] is used to analyze the measured admittances.

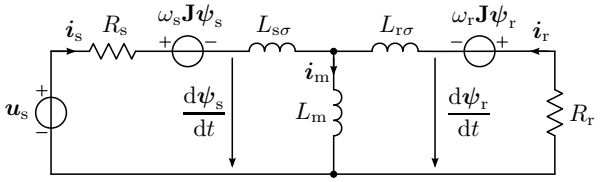


Fig. 1. Dynamic T-equivalent circuit of the induction motor in synchronous reference frame rotating at $\omega_\mathrm{s}$. The slip angular frequency is $\omega_\mathrm{r} = \omega_\mathrm{s} - \omega_\mathrm{m}$.

## II. Induction Motor Model

### A. Large-Signal Model

In a reference frame rotating at the stator angular frequency $\omega_\mathrm{s}$, the induction motor can be described by

$$\frac{\mathrm{d}\boldsymbol{\psi}_\mathrm{s}}{\mathrm{d}t} = \boldsymbol{u}_\mathrm{s} - R_\mathrm{s}\boldsymbol{i}_\mathrm{s} - \omega_\mathrm{s}\mathbf{J}\boldsymbol{\psi}_\mathrm{s} \tag{1a}$$

$$\frac{\mathrm{d}\boldsymbol{\psi}_\mathrm{r}}{\mathrm{d}t} = -R_\mathrm{r}\boldsymbol{i}_\mathrm{r} - (\omega_\mathrm{s} - \omega_\mathrm{m})\,\mathbf{J}\boldsymbol{\psi}_\mathrm{r} \tag{1b}$$

where the stator voltage is denoted by $\boldsymbol{u}_\mathrm{s}$, the stator current by $\boldsymbol{i}_\mathrm{s}$, the rotor current by $\boldsymbol{i}_\mathrm{r}$, the stator flux by $\boldsymbol{\psi}_\mathrm{s}$, and the rotor flux by $\boldsymbol{\psi}_\mathrm{r}$. Real-valued vectors are used, e.g. $\boldsymbol{u}_\mathrm{s} = [u_\mathrm{sd}, u_\mathrm{sq}]^\mathrm{T}$. The stator and rotor resistances are denoted by $R_\mathrm{s}$ and $R_\mathrm{r}$, respectively. The electrical angular speed of the rotor is $\omega_\mathrm{m}$ and the slip angular frequency $\omega_\mathrm{r} = \omega_\mathrm{s} - \omega_\mathrm{m}$. The orthogonal rotation matrix is

$$\mathbf{J} = \begin{bmatrix} 0 & -1 \\ 1 & 0 \end{bmatrix} \tag{2}$$

The stator and rotor fluxes are

$$\boldsymbol{\psi}_\mathrm{s} = L_\mathrm{s}\boldsymbol{i}_\mathrm{s} + L_\mathrm{m}\boldsymbol{i}_\mathrm{r} \tag{3a}$$

$$\boldsymbol{\psi}_\mathrm{r} = L_\mathrm{m}\boldsymbol{i}_\mathrm{s} + L_\mathrm{r}\boldsymbol{i}_\mathrm{r} \tag{3b}$$

where $L_\mathrm{m}$ is the magnetizing inductance. Denoting the stator and rotor leakage inductances by $L_{\mathrm{s}\sigma}$ and $L_{\mathrm{r}\sigma}$, respectively, the stator inductance is $L_\mathrm{s} = L_\mathrm{m} + L_{\mathrm{s}\sigma}$ and the rotor inductance is $L_\mathrm{r} = L_\mathrm{m} + L_{\mathrm{r}\sigma}$. The induction motor model is illustrated by the T-equivalent circuit in Fig. 1, where the magnetizing current is denoted by $\boldsymbol{i}_\mathrm{m}$.

In the following, the main flux and the rotor leakage flux are assumed to be functions of the magnetizing current and the rotor current. The inductances are defined as

$$L_\mathrm{m}(i_\mathrm{m}, i_\mathrm{r}) = \frac{\psi_\mathrm{m}(i_\mathrm{m}, i_\mathrm{r})}{i_\mathrm{m}}, \quad L_{\mathrm{r}\sigma}(i_\mathrm{m}, i_\mathrm{r}) = \frac{\psi_{\mathrm{r}\sigma}(i_\mathrm{m}, i_\mathrm{r})}{i_\mathrm{r}} \tag{4}$$

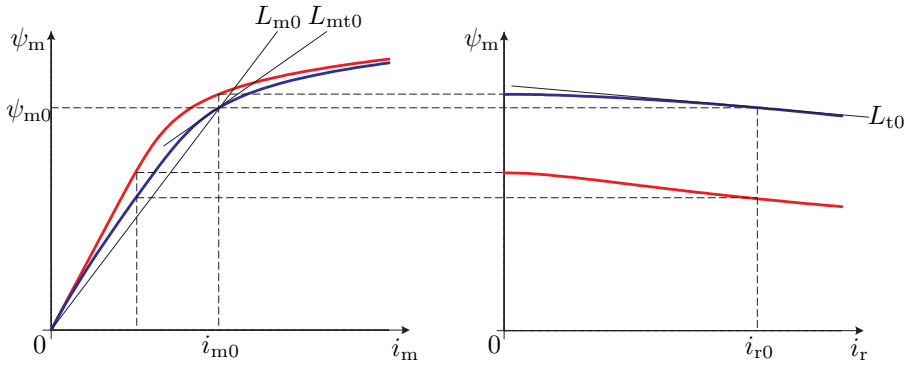


Fig. 2. Typical saturation characteristics of the main flux $\psi_{\mathrm{m}}(i_{\mathrm{m}}, i_{\mathrm{r}})$. In the left-hand side, the main flux is shown as a function of the magnetizing current: the upper curve corresponds to no-load operation (rotor current $i_{\mathrm{r}} = 0$) and the lower curve corresponds to operation under load ($i_{\mathrm{r}} = i_{\mathrm{r0}}$). In the right-hand side, the main flux is shown as a function of the rotor current at two different values of the magnetizing current: the upper curve corresponds to the magnetizing current $i_{\mathrm{m0}}$ in the left-hand side, and the lower curve corresponds to half of this value. The incremental inductances $L_{\mathrm{mt0}} = (\partial\psi_{\mathrm{m}}/\partial i_{\mathrm{m}})_0$ and $L_{\mathrm{t0}} = (\partial\psi_{\mathrm{m}}/\partial i_{\mathrm{r}})_0$, and the operating point inductance $L_{\mathrm{m0}} = \psi_{\mathrm{m0}}/i_{\mathrm{m0}}$ are illustrated in the operating point $\psi_{\mathrm{m0}} = \psi_{\mathrm{m}}(i_{\mathrm{m0}}, i_{\mathrm{r0}})$.

where the magnitudes of the magnetizing and rotor currents are denoted by $i_{\mathrm{m}}$ and $i_{\mathrm{r}}$, respectively, and the magnitudes of the magnetizing and rotor leakage fluxes by $\psi_{\mathrm{m}}$ and $\psi_{\mathrm{r}\sigma}$, respectively. The stator leakage inductance is assumed to be constant for simplicity. Incremental inductances are defined as

$$L_{\mathrm{mt}} = \frac{\partial\psi_{\mathrm{m}}}{\partial i_{\mathrm{m}}}, \quad L_{\mathrm{r}\sigma\mathrm{t}} = \frac{\partial\psi_{\mathrm{r}\sigma}}{\partial i_{\mathrm{r}}}, \quad L_{\mathrm{t}} = \frac{\partial\psi_{\mathrm{m}}}{\partial i_{\mathrm{r}}} = \frac{\partial\psi_{\mathrm{r}\sigma}}{\partial i_{\mathrm{m}}} \tag{5}$$

where the subscript t indicates incremental quantities. The inductance $L_{\mathrm{t}}$ models the mutual saturation between the magnetizing and rotor leakage paths. In Fig. 2, the main flux is shown both as a function of the magnetizing current, keeping the rotor current constant, and as a function of the rotor current, keeping the magnetizing current constant. As the rotor current increases, the main flux decreases. The mutual inductance $L_{\mathrm{t}}$ is, therefore, negative. In the case of no saturation, the incremental inductances are

$$L_{\mathrm{mt}} = L_{\mathrm{m}}, \quad L_{\mathrm{r}\sigma\mathrm{t}} = L_{\mathrm{r}\sigma}, \quad L_{\mathrm{t}} = 0 \tag{6}$$

### *B. Small-Signal Model*

Based on (1)…(4), a small-signal model for the induction motor has been developed [8]. The model includes the saturation of the main-flux and rotor leakage paths, and the mutual saturation between these paths. A state-space representation of the small-signal model can be written as

$$\frac{\mathrm{d}\tilde{\boldsymbol{x}}}{\mathrm{d}t} = \boldsymbol{A}\tilde{\boldsymbol{x}} + \boldsymbol{B}_{\mathrm{s}}\tilde{\boldsymbol{u}}_{\mathrm{s}} + \boldsymbol{b}\tilde{\omega}_{\mathrm{m}} \tag{7}$$

where

$$\tilde{\boldsymbol{x}} = \begin{bmatrix}\tilde{\boldsymbol{\psi}}_{\mathrm{s}} \\ \tilde{\boldsymbol{\psi}}_{\mathrm{r}}\end{bmatrix}, \quad \boldsymbol{B}_{\mathrm{s}} = \begin{bmatrix}\mathbf{I} \\ \mathbf{0}\end{bmatrix}, \quad \boldsymbol{b} = \begin{bmatrix}0 \\ 0 \\ \mathbf{J}\boldsymbol{\psi}_{\mathrm{r0}}\end{bmatrix} \tag{8}$$

Operating-point quantities are marked with the subscript 0, and tilde marks the deviation around the operating point. The identity and zero matrices are

$$\mathbf{I} = \begin{bmatrix}1 & 0 \\ 0 & 1\end{bmatrix}, \quad \mathbf{0} = \begin{bmatrix}0 & 0 \\ 0 & 0\end{bmatrix} \tag{9}$$

The state matrix in (7) is given by

$$\boldsymbol{A} = -\begin{bmatrix}R_{\mathrm{s}}\mathbf{I} & \mathbf{0} \\ \mathbf{0} & R_{\mathrm{r}}\mathbf{I}\end{bmatrix}\boldsymbol{L}^{-1} - \begin{bmatrix}\omega_{\mathrm{s0}}\mathbf{J} & \mathbf{0} \\ \mathbf{0} & \omega_{\mathrm{r0}}\mathbf{J}\end{bmatrix} \tag{10}$$

and based on the assumptions in (4), the inductance matrix becomes

$$\begin{aligned}\boldsymbol{L} = &\begin{bmatrix}L_{\mathrm{s0}}\mathbf{I} & L_{\mathrm{m0}}\mathbf{I} \\ L_{\mathrm{m0}}\mathbf{I} & L_{\mathrm{r0}}\mathbf{I}\end{bmatrix} \\ &+ \frac{L_{\mathrm{mt0}} - L_{\mathrm{m0}}}{i_{\mathrm{m0}}^2}\begin{bmatrix}\boldsymbol{i}_{\mathrm{m0}}\boldsymbol{i}_{\mathrm{m0}}^{\mathrm{T}} & \boldsymbol{i}_{\mathrm{m0}}\boldsymbol{i}_{\mathrm{m0}}^{\mathrm{T}} \\ \boldsymbol{i}_{\mathrm{m0}}\boldsymbol{i}_{\mathrm{m0}}^{\mathrm{T}} & \boldsymbol{i}_{\mathrm{m0}}\boldsymbol{i}_{\mathrm{m0}}^{\mathrm{T}}\end{bmatrix} \\ &+ \frac{L_{\mathrm{r}\sigma\mathrm{t0}} - L_{\mathrm{r}\sigma0}}{i_{\mathrm{r0}}^2}\begin{bmatrix}\mathbf{0} & \mathbf{0} \\ \mathbf{0} & \boldsymbol{i}_{\mathrm{r0}}\boldsymbol{i}_{\mathrm{r0}}^{\mathrm{T}}\end{bmatrix} \\ &+ \frac{L_{\mathrm{t0}}}{i_{\mathrm{m0}}i_{\mathrm{r0}}}\begin{bmatrix}\mathbf{0} & \boldsymbol{i}_{\mathrm{m0}}\boldsymbol{i}_{\mathrm{r0}}^{\mathrm{T}} \\ \boldsymbol{i}_{\mathrm{r0}}\boldsymbol{i}_{\mathrm{m0}}^{\mathrm{T}} & \boldsymbol{i}_{\mathrm{m0}}\boldsymbol{i}_{\mathrm{r0}}^{\mathrm{T}} + \boldsymbol{i}_{\mathrm{r0}}\boldsymbol{i}_{\mathrm{m0}}^{\mathrm{T}}\end{bmatrix}\end{aligned} \tag{11}$$

The last three terms in the inductance matrix are due to the saturation.

The deviation in the stator current can be obtained from the deviation in the fluxes by $\tilde{\boldsymbol{i}}_{\mathrm{s}} = \boldsymbol{C}_{\mathrm{s}}\tilde{\boldsymbol{x}}$, where

$$\boldsymbol{C}_{\mathrm{s}} = \begin{bmatrix}\mathbf{I} & \mathbf{0}\end{bmatrix}\boldsymbol{L}^{-1} \tag{12}$$

As can be seen in (7), the deviations in the fluxes, and thus also the deviations in the stator current, are caused by deviations in the stator voltage and the speed:

$$\tilde{\boldsymbol{i}}_{\mathrm{s}}(s) = \boldsymbol{Y}_{\mathrm{s}}(s)\tilde{\boldsymbol{u}}_{\mathrm{s}}(s) + \boldsymbol{g}(s)\tilde{\omega}_{\mathrm{m}}(s) \tag{13}$$

The small-signal admittance is

$$\boldsymbol{Y}_{\mathrm{s}}(s) = \begin{bmatrix}Y_{\mathrm{dd}}(s) & Y_{\mathrm{dq}}(s) \\ Y_{\mathrm{qd}}(s) & Y_{\mathrm{qq}}(s)\end{bmatrix} = \boldsymbol{C}_{\mathrm{s}}\left(s\mathbf{I}_4 - \boldsymbol{A}\right)^{-1}\boldsymbol{B}_{\mathrm{s}} \tag{14}$$

and the transfer function from the speed to the current is

$$\boldsymbol{g}(s) = \begin{bmatrix}g_{\mathrm{d}}(s) \\ g_{\mathrm{q}}(s)\end{bmatrix} = \boldsymbol{C}_{\mathrm{s}}\left(s\mathbf{I}_4 - \boldsymbol{A}\right)^{-1}\boldsymbol{b} \tag{15}$$

where $\mathbf{I}_4$ denotes a $4 \times 4$ identity matrix.

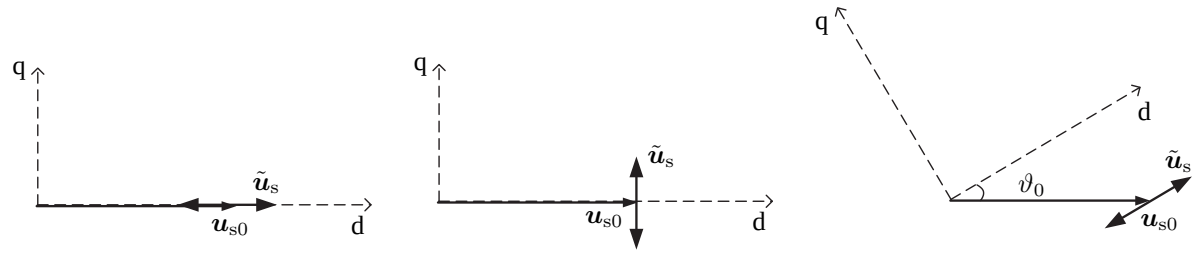


Fig. 3. The direction of the excitation signals $\tilde{\boldsymbol{u}}_\mathrm{s}$ used in the admittance measurement. The excitation signal is injected (a) in the d direction and (b) in the q direction for measuring the admittance as a function of the frequency. In (c), the excitation is injected in the d direction of the reference frame at different values of the angle $\vartheta_0$.

## III. Methods Used for Analysis

If the speed is kept constant, the small-signal admittance can be measured by superimposing signals on the operating point stator voltage. When the voltage signal is injected in the d direction and the voltage deviation in the q direction is zero, the admittance elements $Y_\mathrm{dd}$ and $Y_\mathrm{qd}$ can be calculated according to

$$Y_\mathrm{dd}(s) = \frac{\tilde{i}_\mathrm{sd}(s)}{\tilde{u}_\mathrm{sd}(s)}, \quad Y_\mathrm{qd}(s) = \frac{\tilde{i}_\mathrm{sq}(s)}{\tilde{u}_\mathrm{sd}(s)} \tag{16}$$

Correspondingly, when the voltage signal is injected in the q direction and the voltage deviation in the d direction is zero, the elements $Y_\mathrm{dq}$ and $Y_\mathrm{qq}$ are obtained,

$$Y_\mathrm{dq}(s) = \frac{\tilde{i}_\mathrm{sd}(s)}{\tilde{u}_\mathrm{sq}(s)}, \quad Y_\mathrm{qq}(s) = \frac{\tilde{i}_\mathrm{sq}(s)}{\tilde{u}_\mathrm{sq}(s)} \tag{17}$$

In the case of no saturation, $Y_\mathrm{dd}(s) = Y_\mathrm{qq}(s)$ and $Y_\mathrm{dq}(s) = -Y_\mathrm{qd}(s)$.

The transfer function $\boldsymbol{g}(s)$ can be measured by producing speed deviations at different frequencies and measuring the corresponding deviations in the stator current. During this measurement, no voltage excitation signals are injected. The transfer function $\boldsymbol{g}$ is

$$\boldsymbol{g}(s) = \frac{\tilde{\boldsymbol{i}}_\mathrm{s}(s)}{\tilde{\omega}_\mathrm{m}(s)} \tag{18}$$

Significant speed deviations can occur at low signal frequencies. The small-signal admittance can then be measured only if the transfer function $\boldsymbol{g}(s)$ is known. To calculate the admittance, the corrected stator current deviation

$$\tilde{\boldsymbol{i}}'_\mathrm{s}(s) = \tilde{\boldsymbol{i}}_\mathrm{s}(s) - \boldsymbol{g}(s)\tilde{\omega}_\mathrm{m}(s) \tag{19}$$

should be used in (16) and (17) instead of the measured stator current deviation $\tilde{\boldsymbol{i}}_\mathrm{s}(s)$.

In this paper, the small-signal admittance is studied using FEA and laboratory experiments. The two-dimensional, time-stepping FEA [9] includes the magnetic saturation of the iron core and the eddy currents in the cage winding of the rotor. End effects are modeled by resistances and inductances in the stator and rotor circuits. The small-signal admittance is analyzed as a function of both the frequency and the direction of the excitation signal. To obtain the admittance as a function of the frequency, a voltage pulse [10]

$$\tilde{u}_\mathrm{s} = \begin{cases} u_\delta \sin^2(\omega_\delta t), & 0 \le t \le 1/(2\omega_\delta) \\ 0, & \text{otherwise} \end{cases} \tag{20}$$

having the amplitude $u_\delta$ and angular frequency $\omega_\delta$, was fed to a selected direction in the synchronous reference frame in the FEA. The results of time-stepping computations were transformed to the frequency domain using DFT. The admittances at all frequencies of interest were thus obtained with a minimum number of finite element computations.

To reduce the influence of the measurement noise, the pulse test was not used in the laboratory experiments. Instead, the admittance was measured at several frequencies, one at a time, using sinusoidal voltage signals

$$\tilde{u}_\mathrm{s} = u_\mathrm{c} \sin(\omega t) \tag{21}$$

The excitation signals were injected in two perpendicular directions, first in the d direction in a reference frame aligned with the operating-point stator voltage, as in Fig. 3(a), and then in the q direction as in Fig. 3(b). All four elements in the admittance matrix were calculated according to (16) and (17), and the analytical model (14) was fitted to the admittance [8]. In the data fitting, the stator leakage inductance was fixed to zero. In the case of no saturation, the total leakage inductance can be identified, but the stator and rotor leakage inductances cannot be distinguished from each other. As the motor saturates, the leakage inductances can, in theory, be identified separately [11]. In practice, however, it is difficult to obtain reliable information because of measurement noise. For the comparison of the results obtained from FEA and laboratory experiments, setting the value of the stator leakage inductance to zero is a convenient choice.

The effect of the direction of the excitation signal on the small-signal admittance was also analyzed. The sinusoidal voltage signal in (21) was used both in the FEA and in the laboratory experiments. The voltage signal was injected in the d direction of the reference frame illustrated in Fig. 3(c), and the admittances $Y_\mathrm{dd}$ and $Y_\mathrm{qd}$ were calculated. The electrical angle $\vartheta_0$ of the reference frame with respect to the operating-point stator voltage $\boldsymbol{u}_\mathrm{s0}$ was varied in steps of $10^\circ$ in the range of $0^\circ \ldots 180^\circ$. The small-signal admittance was thus obtained as a function of the angle of the excitation signal.

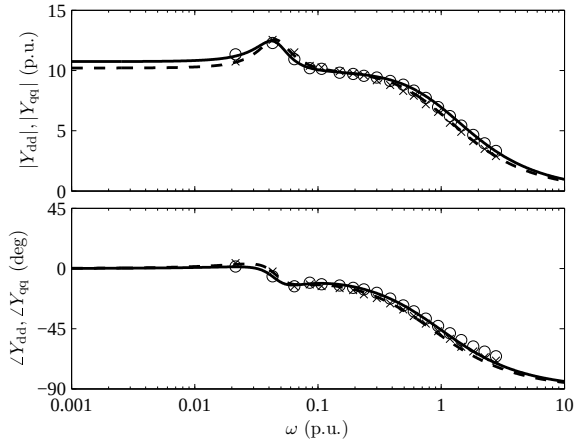


(a)

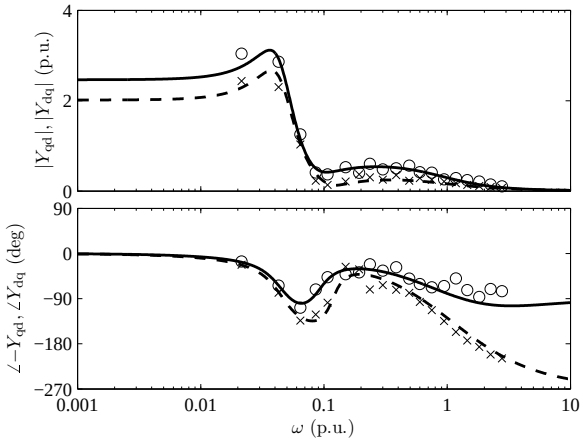


(b)

Fig. 4. Small-signal admittance from FEA (circles and crosses) and from data fitting (solid and dashed lines) as a function of the angular frequency $\omega$ of the excitation signal when the rotor is locked: (a) $Y_{\rm dd}$ shown by circles and solid lines, $Y_{\rm qq}$ shown by crosses and dashed lines; (b) $Y_{\rm qd}$ shown by circles and solid lines and $Y_{\rm dq}$ shown by crosses and dashed lines.

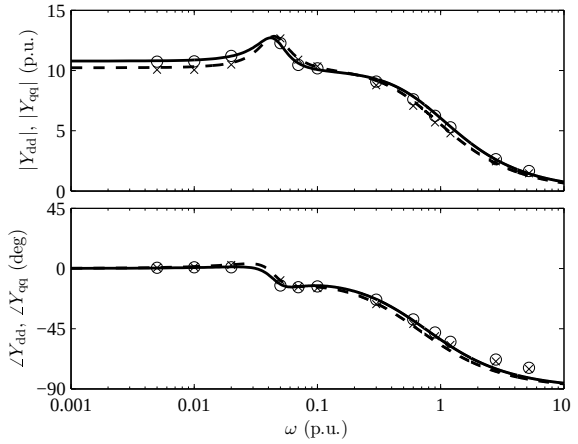


(a)

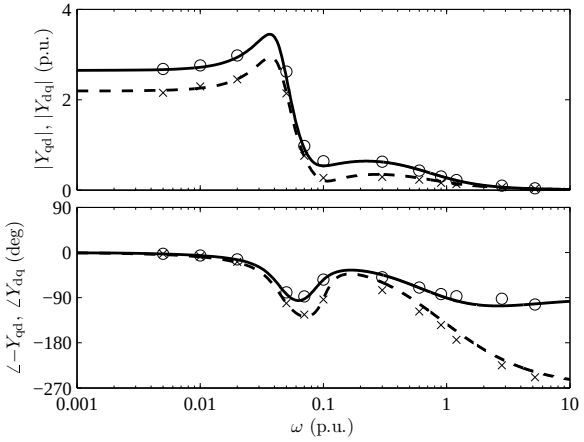


(b)

Fig. 5. Measured (circles and crosses) and fitted (solid and dashed lines) small-signal admittance as a function of the angular frequency $\omega$ of the excitation signal when the rotor is locked. The curves are explained as in Fig 4.

## IV. Results

A 2.2-kW induction motor was used in the FEA and laboratory experiments. The motor is equipped with closed and skewed rotor slots, and its rated values are: voltage 400 V; current 5 A; frequency 50 Hz; speed 1436 r/min; and torque 14.6 Nm. In the laboratory experiments, the motor was fed by a frequency converter controlled by a dSpace DS1103 PPC/DSP board. The motor was loaded by a servo motor, the moment of inertia of the set-up being 0.0155 kgm$^2$.

The FEA and the laboratory experiments were performed in two operating points. In the first case, the rotor was locked to ensure that variations in the speed would not affect the result; the stator frequency was equal to the rated slip frequency (0.0426 p.u.) and the stator current equalled the rated current. In the second case, the rotor was rotating, and the speed, current and slip frequency were equal to the rated values. The laboratory experiments were performed as the motor was at the room temperature, but the FEA corresponds to the rated temperature.

### A. Locked Rotor

In the locked-rotor case, the amplitude of the voltage pulse (20) used in the FEA was 0.02 p.u. (6.5 V), the angular frequency $\omega_\delta = 4$ p.u., and the duration time was 25 ms. The small-signal admittances obtained from the FEA and the measurements are shown by markers in Figs. 4 and 5, respectively, as a function of the excitation frequency. It can be seen that the computed and measured results correspond well to each other, but they differ more at high excitation frequencies than at low excitation frequencies.

The curves in Figs. 4 and 5 show the small-signal admittances obtained from the fitted analytical models. The model seems to fit well to the data. If no saturation were present, $Y_{\rm dd} = Y_{\rm qq}$ and $Y_{\rm dq} = -Y_{\rm qd}$, and the solid and dashed curves would be equal. The fitted parameter values are given in Table I. The magnetizing and rotor currents are calculated based on the fitted parameters and the operating-point data. It is to be noted that the analytical model does not

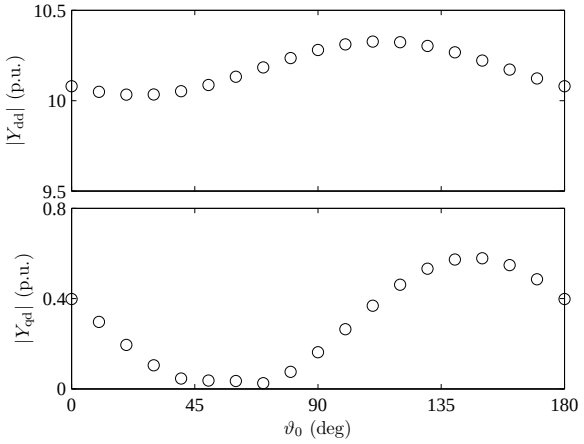


(a)

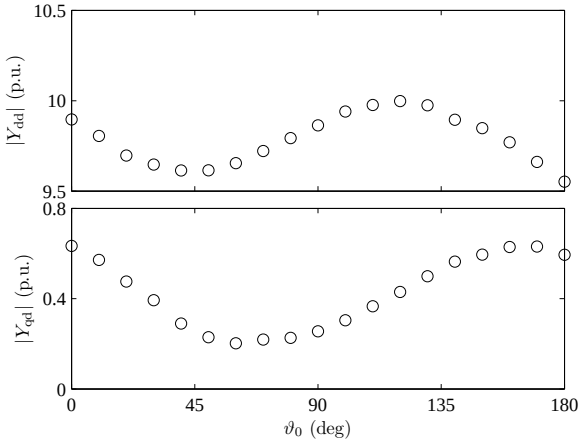


(b)

Fig. 6. Small-signal admittances $|Y_{\mathrm{dd}}(s)|$ and $|Y_{\mathrm{dq}}(s)|$ obtained from (a) FEA and (b) measurements as a function of the angle of the excitation signal. The frequency of the injected signal is 0.1 p.u. and the amplitude 0.02 p.u. The stator frequency equals the rated slip frequency and the rotor is locked.

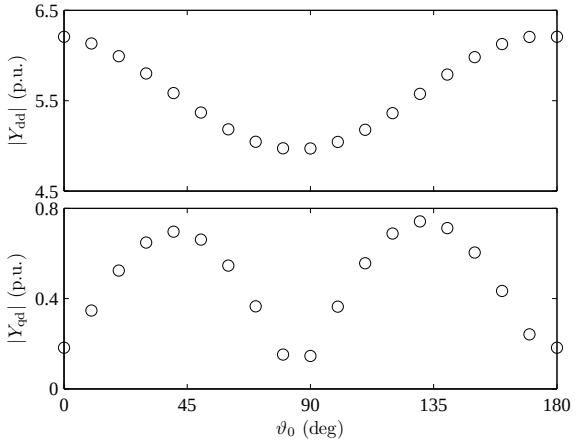


(a)

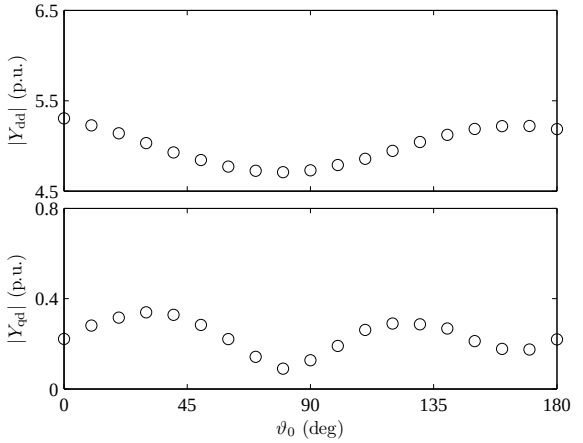


(b)

Fig. 7. Small-signal admittances $|Y_{\mathrm{dd}}(s)|$ and $|Y_{\mathrm{dq}}(s)|$ obtained from (a) FEA and (b) measurements as a function of the angle of the excitation signal. The frequency of the injected signal is 1.2 p.u. and the amplitude 0.025 p.u. The stator frequency equals the rated slip frequency and the rotor is locked.

TABLE I
FITTED PER-UNIT PARAMETERS IN THE LOCKED-ROTOR OPERATING POINT

| | FEA | Measurements |
|---|---|---|
| $L_{\mathrm{m0}}$ | 1.76 | 1.93 |
| $L_{\mathrm{r}\sigma 0}$ | 0.131 | 0.168 |
| $L_{\mathrm{s}\sigma 0}$ | 0 | 0 |
| $R_{\mathrm{s}}$ | 0.0667 | 0.0645 |
| $R_{\mathrm{r}}$ | 0.0394 | 0.0416 |
| $L_{\mathrm{mt0}}$ | 1.18 | 1.29 |
| $L_{\mathrm{r}\sigma\mathrm{t0}}$ | 0.116 | 0.148 |
| $L_{\mathrm{t0}}$ | $-0.0576$ | $-0.0553$ |
| $\boldsymbol{i}_{\mathrm{m0}}$ | $0.445\angle{-67}^\circ$ | $0.426\angle{-67}^\circ$ |
| $\boldsymbol{i}_{\mathrm{r0}}$ | $0.845\angle{-165}^\circ$ | $0.829\angle{-167}^\circ$ |

include the frequency dependence of the skin effect in the rotor conductors. This phenomenon could be taken into account by adding a second rotor circuit to the model [12].

In Fig. 6, the admittances are shown as a function of the angle of the reference frame at the excitation frequency 0.1 p.u. (5 Hz). The amplitude $u_{\mathrm{c}}$ of the injected voltage was 0.02 p.u. Fig. 7 shows the admittances at the frequency of 1.2 p.u. (60 Hz). The amplitude of the injected voltage was here increased to 0.025 p.u. The amplitude of the deviation in the stator current was then approximately the same at both frequencies. The influence of the saturation is now seen as a variation of the admittance as a function of the angle. In the case of no saturation, horizontal lines would be obtained.

Comparing the admittances obtained from measurements and FEA in Figs. 6 and 7, it can be seen that the curves have similar shapes, but the amplitudes are different. Particularly at the frequency of 1.2 p.u., the variation in the admittance is much larger in the FEA than in the measurements. According to the analytical model, the variation in the admittance at high frequencies as a function of the angle is mostly affected by the saturation of the rotor leakage flux. The difference between the parameters $L_{\mathrm{r}\sigma 0}$ and $L_{\mathrm{r}\sigma\mathrm{t0}}$ has a large impact on the admittance variation, whereas the influence of other parameters included in the small-signal model is small. The

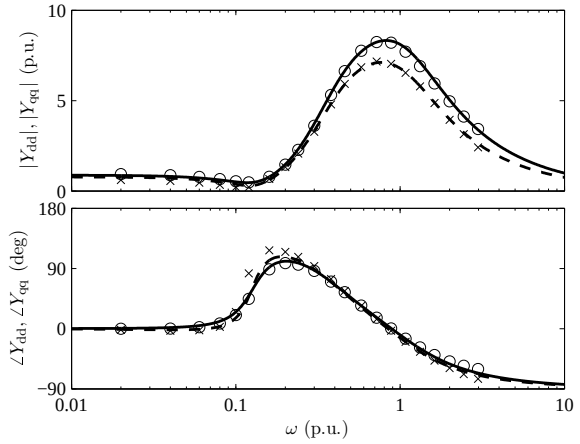


(a)

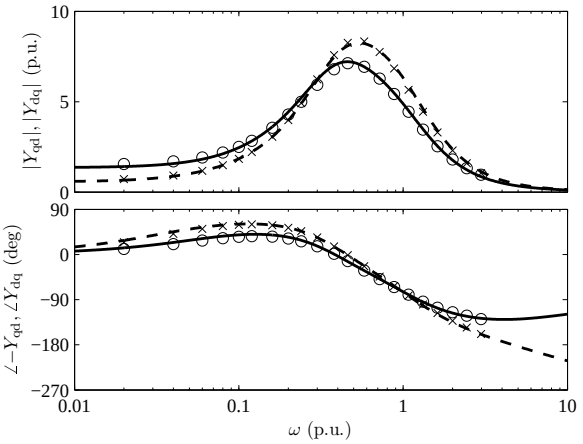


(b)

Fig. 8. The small-signal admittance obtained from FEA as a function of the angular frequency $\omega$ of the excitation signal in the rated operating point. The curves are explained as in Fig. 4.

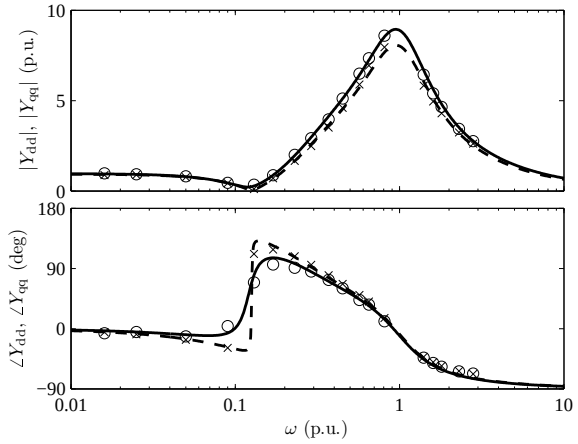


(a)

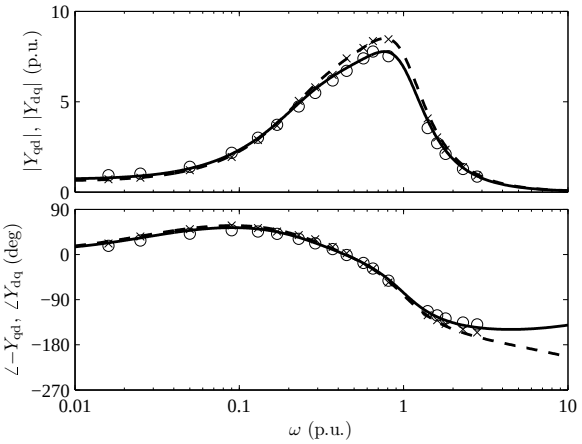


(b)

Fig. 9. The small-signal admittance obtained from laboratory experiments as a function of the angular frequency $\omega$ of the excitation signal in the rated operating point. The curves are explained as in Fig. 4.

larger the difference between $L_{\mathrm{r}\sigma 0}$ and $L_{\mathrm{r}\sigma\mathrm{t}0}$ is, the larger is the variation in the admittance.

### *B. Rated Operating Point*

Figs. 8 and 9 depict the small-signal admittances of a rotating motor; the admittances obtained from the FEA and the measurements in the rated operating point are shown by markers as a function of the excitation frequency. The amplitude of the voltage pulse (20) in the FEA was 0.05 p.u. At frequencies below 1 p.u., the deviations in the speed were rather large. Therefore, the transfer function from the speed to the stator current was first measured, and the compensation of the speed deviations (19) was used at those frequencies. It can be seen that the computed and measured results correspond to each other less well than those in the locked-rotor case.

The fitted parameters are shown in Table II. The differences between the parameter values obtained from the FEA and the measurements are more pronounced than those obtained in the locked-rotor case. Particularly the difference in the incremental magnetizing inductance $L_{\mathrm{mt}0}$ is large. It corresponds to the difference in the magnetizing current $\boldsymbol{i}_{\mathrm{m}0}$. It is to be noted that the incremental magnetizing inductance is sensitive to measurement errors at low frequencies. At these frequencies, the measured admittances are not only affected by the measurement noise in the stator current and stator voltage, but also by the measurement noise in the speed.

In Fig. 10, the admittances are shown as a function of

TABLE II
FITTED PER-UNIT PARAMETERS IN THE RATED OPERATING POINT

| | FEA | Measurements |
|---|---|---|
| $L_{\mathrm{m}0}$ | 1.87 | 1.91 |
| $L_{\mathrm{r}\sigma 0}$ | 0.171 | 0.176 |
| $L_{\mathrm{s}\sigma 0}$ | 0 | 0 |
| $R_{\mathrm{s}}$ | 0.0787 | 0.0648 |
| $R_{\mathrm{r}}$ | 0.0524 | 0.0417 |
| $L_{\mathrm{mt}0}$ | 0.680 | 1.53 |
| $L_{\mathrm{r}\sigma\mathrm{t}0}$ | 0.110 | 0.156 |
| $L_{\mathrm{t}0}$ | $-0.0403$ | $-0.0648$ |
| $\boldsymbol{i}_{\mathrm{m}0}$ | $0.503\angle -87°$ | $0.431\angle -88°$ |
| $\boldsymbol{i}_{\mathrm{r}0}$ | $0.759\angle 175°$ | $0.806\angle 172°$ |

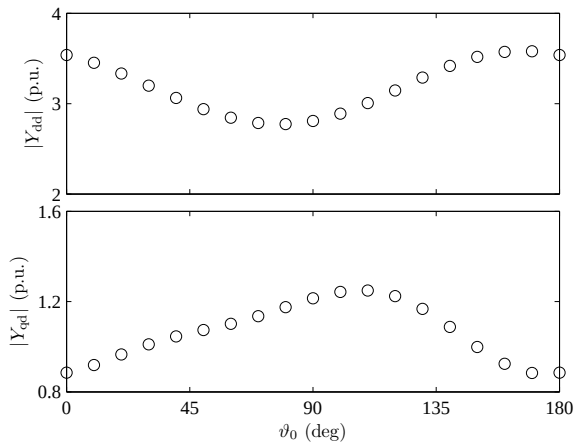


(a)

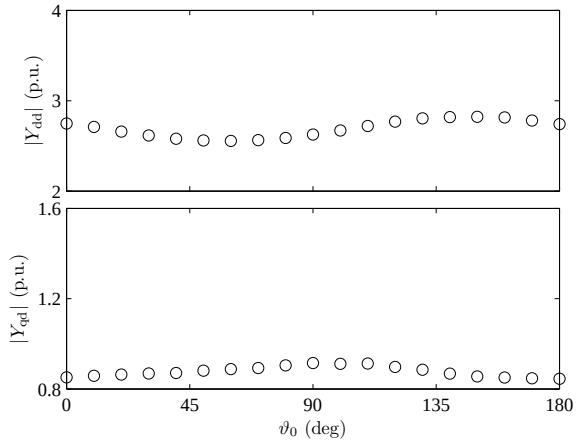


(b)

Fig. 10. Small-signal admittances $|Y_{\mathrm{dd}}(s)|$ and $|Y_{\mathrm{dq}}(s)|$ obtained by (a) FEA and (b) measurements as a function of the angle of the operating-point stator voltage. The frequency of the injected signal is 2.8 p.u. and the amplitude 0.025 p.u. The stator frequency, current and the slip equal their rated values.

the angle of the reference frame at the excitation frequency 2.8 p.u. The same observations can be made as at the higher frequency in the locked-rotor case (Fig. 7): the variations in the admittances obtained from the FEA are rather large, but the variations in the measured admittance are much smaller.

## V. Discussion

The small-signal admittances obtained from the FEA and the laboratory experiments correspond well to each other, particularly in the locked-rotor case. However, at frequencies above the rated frequency, differences in the results are observed. Possible reasons for these differences are discussed in the following.

The rotor leakage flux saturates because of closed and skewed rotor slots. The axial variation of the rotor flux due to skewed rotor slots is not taken into account in the two-dimensional FEA, but it is present in the real motor. The iron bridges closing the rotor slots at the outer surface of the rotor are very thin. Due to manufacturing tolerances, the actual thickness of the iron bridges may differ from its nominal value considerably. In addition, the magnetic properties of punched laminations deteriorate in a thin layer at the surfaces, which is difficult to take into account in the FEA.

Due to the skin effect, the rotor resistance increases and the rotor leakage inductance decreases with the frequency. The skin effect in the rotor conductors is included in the FEA, but inaccuracies regarding the geometry and material characteristics can cause differences with respect to the measurements. The influence of the skin effect on the end-winding resistance and inductance is not included in the finite element model used, and the iron losses are also omitted. A further source of inaccuracy, significant at high frequencies, are the surface currents due to imperfect insulations between the iron laminations at the machined rotor surface.

In this investigation, the stator resistance used in the FEA differs from the resistance in the laboratory experiments as the laboratory experiments were performed at room temperature, but the finite element model corresponds to a motor at the rated temperature. The flux level in the FEA thus differs from that in the measurements, leading to differences in the inductance values.

The measured curves are also affected by the temperature rise during the measurements, which can easily be observed when the admittance is measured as a function of the direction of the excitation signal. Due to the increased resistances, the admittances at the angle $180^\circ$ differ a few percent from those at the angle $0^\circ$. This difference can be seen clearly in the low-frequency measurement of $|Y_{\mathrm{dd}}|$ presented in Fig. 6(b). The measurement at this frequency lasts for about ten minutes while the measurements at the higher frequencies in Fig. 7(b) and Fig. 10(b) last for about seven minutes.

## VI. Conclusions

The small-signal admittances of a 2.2-kW induction motor were studied by the means of the finite element analysis and measurements, and a small-signal model was used for analyzing and comparing the admittances. The small-signal model, including the saturation, fits well to the obtained data. Due to the saturation, the small-signal admittance varies as a function of the direction of the excitation signal. In the locked-rotor case, the admittances obtained from the finite element analysis correspond well to the measured admittances, but differences arise at higher frequencies. These differences can be explained by simplifications and approximations included in the two-dimensional, time-stepping finite element method used. When the rotor is rotating, low-frequency excitation signals can cause variations in the rotor speed, making it more difficult to measure the small-signal admittances.

## VII. Acknowledgement

The authors gratefully acknowledge the financial support given by ABB Oy.

## References

[1] A. Yahiaoui and F. Bouillault, "Saturation effect on the electromagnetic behaviour of an induction machine," *IEEE Trans. Magn.*, vol. 31, no. 3, pp. 2036–2039, May 1995.

[2] C. Gerada, K. Bradley, M. Sumner, and P. Sewell, "Evaluation and modelling of cross saturation due to leakage flux in vector controlled induction machines," in *Proc. IEEE IEMDC'03*, vol. 3, San Diego, CA, June 2003, pp. 1983–1989.

[3] M. Aime, M. Degner, and R. Lorenz, "Saturation measurements in AC machines using carrier signal injection," in *Conf. Rec. IEEE-IAS Annu. Meeting*, vol. 1, St. Louis, MO, Oct. 1998, pp. 159–166.

[4] F. Briz, M. Degner, A. Diez, and R. Lorenz, "Measuring, modeling and decoupling of saturation-induced saliencies in carrier-signal injection based sensorless AC drives," *IEEE Trans. Ind. Appl.*, vol. 37, no. 5, pp. 1356–1364, Sept./Oct. 2001.

[5] F. Blaschke, J. van der Burgt, and A. Vandenput, "Sensorless direct field orientation at zero flux frequency," in *Conf. Rec. IEEE-IAS Annu. Meeting*, vol. 1, San Diego, CA, Oct. 1996, pp. 189–196.

[6] R. J. Kerkman, J. D. Thunes, T. M. Rowan, and D. W. Schlegel, "A frequency-based determination of transient inductance and rotor resistance for field commissioning purposes," *IEEE Trans. Ind. Appl.*, vol. 32, no. 3, pp. 577–584, May/June 1996.

[7] M. Sumner and G. M. Asher, "Autocommissioning for voltage-referenced voltage-fed vector-controlled induction motor drives," *IEE Proc. B, Electr. Power Appl.*, vol. 140, no. 3, pp. 187–200, May 1993.

[8] M. Hinkkanen, A.-K. Repo, M. Cederholm, and J. Luomi, "Small-signal modelling of saturated induction machines with closed or skewed rotor slots," in *Conf. Rec. IEEE-IAS Annu. Meeting*, New Orleans, LA, Sept. 2007, pp. 1200–1206.

[9] A. Arkkio, "Analysis of induction motors based on the numerical solution of the magnetic field and circuit equations," Ph.D. dissertation, Dept. Elect. Commun. Eng., Helsinki Univ. Tech., Espoo, Finland, Dec. 1987.

[10] A. Repo and A. Arkkio, "Numerical impulse response test to estimate circuit-model parameters for induction machines," *IEE Proc. Electr. Power Appl.*, vol. 153, no. 6, pp. 883–890, Nov. 2006.

[11] J. Melkebeek and D. Novotny, "The influence of saturation on induction machine drive dynamics," *IEEE Trans. Ind. Appl.*, vol. 19, no. 5, pp. 671–681, Sept./Oct. 1983.

[12] M. Hinkkanen, A.-K. Repo, M. Cederholm, and J. Luomi, "Small-signal model for saturated deep-bar induction machines," in *Proc. EPE 2007*, Aalborg, Denmark, Sept. 2007.